Research Square

Preprints are preliminary reports that have not undergone peer review.
They should not be considered conclusive, used to inform clinical practice,
or referenced by the media as validated information.

Exploration of High-Entropy Engineered Skutterudite as a Route to Tunable Electronic and Magneto-Thermal Functionalities

Micheal O Ogunbunmi

mogunbun@xula.edu

Xavier University of Louisiana https://orcid.org/0000-0002-5340-9198

Research Article

Keywords: High-entropy alloy, High-entropy intermetallics, Caged structures, Skutterudites, Magneto-thermal functionalities

Posted Date: October 6th, 2026

DOI: https://doi.org/10.21203/rs.3.rs-11262700/v1

License: This work is licensed under a Creative Commons Attribution 4.0 International License.
Read Full License

Additional Declarations: The authors declare no competing interests.

Exploration of High-Entropy Engineered Skutterudite as a Route to Tunable Electronic and Magneto-Thermal Functionalities

Michael O. Ogunbunmi

Physics and Engineering Department, Xavier University of Louisiana, 1 Drexel Drive, New Orleans, 70125, Louisiana, United States.

Contributing authors: mogunbun@xula.edu;

Abstract

High-entropy alloys have in recent years emerged as a transformative materials design paradigm offering vast compositional space to explore various properties of interest. However, their exploration has largely focused on simple metallic solid solutions. Here, we extend the high-entropy concept to complex caged intermetallic systems, specifically the Skutterudites, $\boldsymbol{RT_4X_{12}}$ ($\boldsymbol{R}$ = rare-earth or alkaline-earth filler atom, $\boldsymbol{T}$ = transition metal, $\boldsymbol{X}$ = pnictogen), as a new viable platform for entropy-stabilized electronic materials. The Skutterudite structure provides multiple crystallographic sublattices, allowing controlled configurational disorder while preserving structural integrity. Using the Special Quasirandom Structure (SQS) approach coupled with density functional theory studies to predict phase stability and electronic properties of the novel high-entropy composition, $\mathbf{(La_{0.25}Ce_{0.25}Pr_{0.25}Nd_{0.25})(Fe_{0.5}Co_{0.5})_4(As_{0.25}Se_{0.25}Sb_{0.25}Te_{0.25})_{12}}$. Its formation energy is -0.17495 eV/atom, and the configurational entropy, $\boldsymbol{S_{conf}}$ = 1.223R/f.u., which is significant for a material that reflects substantial multisublattice chemical disorder and strong site ordering. The As/Se/Sb/Te sublattice has a lattice mismatch of 7.37%, a feature which is attributed to the observed local lattice strain and could be beneficial for improved thermodynamic stability. The magnetism is driven by the Fe/Co sublattice and is itinerant in nature. Electronic structure calculations indicate features reminiscent of metals or semimetals, and the band structure reveals broadened electronic bands with the loss of sharp Bloch character. These results indicate that Skutterudites exhibit exceptional tolerance to multicomponent site mixing, with formation energies remaining within the stable regime. The lattice distortion coupled with

alloy disorder scattering, impurity scattering, and inherent structural intricacy are expected to strongly suppress lattice thermal conductivity.

Keywords: High-entropy alloy, High-entropy intermetallics, Caged structures, Skutterudites, Magneto-thermal functionalities

1 Introduction

High entropy alloys (HEAs) have in recent times gained significant attention due to their exceptional potential for applications in thermoelectrics, catalysis, energy storage, superconductivity, and magneto-thermal technologies.[1] Because of their high configurational entropy and vast compositional design space, HEAs exhibit excellent thermal stability and highly tunable electronic, thermal, and magnetic properties that provide unprecedented opportunities to tailor material performance to meet specific technological needs.[2] Several modern energy technologies often require materials that simultaneously possess multiple functional properties. For example, excellent thermoelectric properties are often favored by low lattice thermal conductivity, high Seebeck coefficient, high electrical conductivity, and high carrier concentration, among others.[3] Catalysis, on the other hand, requires a high density of active sites, a low activation energy barrier, high electrical conductivity, and the ability to easily transfer a charge as well as optimal adsorption energy.[4] However, conventional materials often exhibit certain trade-offs between these properties since improving one property can degrade another, as in the case of thermoelectrics. To this end, HEAs design offers a new paradigm by introducing configurational disorder to engineer material properties beyond the limits of conventional alloying.

Recent advances in high-entropy thermoelectric materials [5, 6] have demonstrated their exceptional potential for energy conversion, leveraging configurational disorder, lattice distortion, and entropy-driven stabilization to achieve ultralow thermal conductivity and enhanced electronic transport. For example, the $AgSnSbSe_{3-x}Te_x$[7] system exemplifies how high-entropy engineering can decouple thermal and electronic transport. The 50:50 composition ($AgSnSbSe_3$) forms a cation-disordered rock-salt structure with intrinsically low lattice thermal conductivity ($\sim$ 0.47 W m^{-1} K^{-1} at 673 K) due to synergistic phonon scattering mechanisms. Further Te alloying creates a quinary high-entropy solid solution ($AgSnSbSe_{1.5}Te_{1.5}$), achieving glass-like thermal conductivity ($\sim$ W m^{-1} K^{-1} and a peak zT of 1.14 via multiband convergence. $AgMnGeSbTe_4$ [8], on the other hand, leverages random cation disorder to induce strong lattice distortion, yielding ultralow κ_l ($\sim$ 0.54 W m^{-1} K^{-1} at 600 K) and a high-power factor (10.36 μW m^{-1} K^{-1}). The precipitation of Ag_8GeTe_6 further enhances zT to 1.27 by selectively scattering low-energy holes and phonons. In the $AgMnGePbSbTe_5$ [9] system, the introduction of nanotwins is used to simultaneously optimize thermoelectric and mechanical properties. Here, configurational entropy reduces stacking fault energy, enabling dense nanotwin boundaries that scatter phonons, while dislocations enhance mechanical strength (flexural strength: 82 MPa). Coupled with Ag_2Te nanoprecipitates, the system achieves a record zT of 2.46 at

750 K. In other systems, such as $AgSbPbSnGeTe_5$[10], the approach of multiband convergence via High-Entropy Design is used to achieve a peak zT of 1.75 at 723 K. Lattice distortion and atomic disorder further suppress κ_l, showcasing entropy as a tool for band structure engineering. It is noted that other interesting results have been reported in several other instances. [11–13] It should be noted that despite progress, critical challenges persist. The exploration of their vast composition space remains bottlenecked by low-throughput methods, and no unified framework yet connects entropy-driven disorder, defect engineering, and charge/heat transport optimization. Similarly, superconducting transition have also been reported in $Ta_{34}Nb_{33}Hf_8Zr_{14}Ti_{11}$ [14], $(NbTa)_{0.67}(MoHfW)_{0.33}$ [15], $Re_{0.56}Nb_{0.11}Ti_{0.11}Zr_{0.11}Hf_{0.11}$ [16], $AgInSnPbBiTe_5$ [17] and in many other phases. [18–24]. In other reports, AuAgPtPdCu was used to achieve the catalytic conversion of CO2 into gaseous hydrocarbons. [25] $Pt_{18}Ni_{26}Fe_{15}Co_{14}Cu_{27}/C$ also shows excellent electrocatalytic performance for the hydrogen evolution reaction and methanol oxidation reaction. [26]. In other instances, HEAs have been explored for hydrogen storage applications [27, 27–30] and other functional materials applications. [31, 32] However, most high-entropy research initiatives have focused largely on simple metallic alloys, leaving ordered caged intermetallic compounds such as Skutterudites, clathrates, filled cage compounds, and other related materials largely unexplored.[33–37] Importantly, our current understanding of HEAs is largely based on face-centered cubic (FCC), body-centered cubic (BCC), and hexagonal close-packed (HCP) alloys. These classical class of HEAs have been extensively explored and studied and continues to provide a fertile ground to explore new phases due to their vast compositional space ($\sim 10^6$ possible quinary systems).[5] In contrast, the fundamental principles governing configurational entropy in ordered caged intermetallic compounds remain largely unexplored. Consequently, the mechanisms by which entropy stabilizes these complex crystal structures and influences their physical properties are not well understood. Caged intermetallic compounds offer an exceptional platform for exploring the fundamental science of entropy engineering. Their inherently complex crystal architectures, multiple crystallographic sublattices, low lattice thermal conductivity, and guest-atom ("rattler") dynamics provide multiple degrees of freedom for independently tuning phonon, electron, spin, and defect interactions. These characteristics make caged compounds ideal model systems for investigating how configurational entropy can be used as a new design variable to control structure–property relationships. Beyond improving thermoelectric performance, this approach has the potential to establish broadly applicable design principles for multifunctional materials exhibiting coupled thermal, electronic, and magnetic functionalities.

In this study, we computationally explore the development of high-entropy intermetallic compounds (HEICs) starting from the extensively studied Skutterudite $CeFe_4Sb_{12}$ compound.[38–46] Our studies provide an opportunity to explore the various magneto-thermal functionalities that can be explored in this type of material, where the various degrees of freedom present provide a rich cocktail that can be leveraged for tuning various properties toward tailored applications. In this manuscript, we will refer to the reported material

as $(La_{0.25}Ce_{0.25}Pr_{0.25}Nd_{0.25})(Fe_{0.5}Co_{0.5})_4(As_{0.25}Se_{0.25}Sb_{0.25}Te_{0.25})_{12}$, or simply as HEIC for brevity.

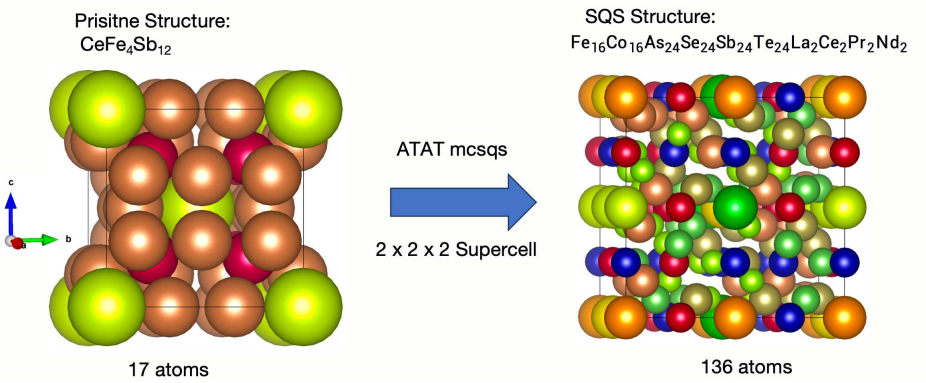


Fig. 1 Schematic illustration of the pristine $CeFe_4Sb_{12}$ and the Special Quasitandom Structure (SQS) model based on $2 \times 2 \times 2$ supercell.

2 Experimental methods

The reported high-entropy cage structure was modeled using the Special Quasirandom Structure (SQS) approach, as implemented in the Alloy Theoretic Automated Toolkit (ATAT). [47] The SQS method constructs a finite periodic supercell whose correlation functions closely reproduce those of an ideal, infinitely large random alloy. Starting with the primitive cell structure of the parent compound $CeFe_4Sb_{12}$ (Space group: $Im\bar{3}$), with three distinct crystallographic sites and having 17 atoms, we created a $2 \times 2 \times 2$ supercell using the gensqs utility to represent the random occupation of the desired sublattice while maintaining the crystallographic framework of the host material. We note that several other candidate supercells of varying sizes were also generated; however, the one with 136 atoms was favored in order to minimize finite-size effects while remaining computationally tractable for subsequent density functional theory (DFT) calculations. The generated supercell preserved the parent lattice symmetry and provided sufficient configurational freedom to approximate a random solid solution. The various sites designated for alloying were assigned variable occupations corresponding to the target elemental compositions as follows: The 136-atom supercell is made up of 8, 32, and 96 atoms for the Ce, Fe, and Sb sublattice sites, respectively, based on the constraints of their respective Wyckoff positions. For the Ce sublattice, the supercell is composed of La, Ce, Pr, and Nd, each with equal concentrations of 0.25 and an equal number of atoms. For the Fe sublattice, it is composed of Fe and Co in equal concentrations of 0.50 and equal number of atoms. Similarly, the Sb sublattice is composed of As, Se, Sb, and Te in equal concentrations and number of atoms. The obtained composition following this approach is $Fe_{16}Co_{16}As_{24}Se_{24}Sb_{24}Te_{24}La_2Ce_2Pr_2Nd_2$ which is equivalent to the normalized composition of $(La_{0.25}Ce_{0.25}Pr_{0.25}Nd_{0.25})(Fe_{0.5}Co_{0.5})_4(As_{0.25}Se_{0.25}Sb_{0.25}Te_{0.25})_{12}$

Additionally, pair cluster interactions were analyzed using the corrdump utility to determine the nearest-neighbor shell distances and the corresponding pair-distance histogram. The first three nearest-neighbor shells were identified at distances of 0.3205, 0.3766, and 0.3841 (normalized lattice units) and based on the histogram (See SI Fig 1), a pair correlation cutoff of 0.4065 was selected, ensuring that pair correlations up to the third nearest-neighbor shell were included in the optimization. This cutoff corresponds to 68 pair instances within the 136-atom supercell, thus providing an adequate statistical representation of the random alloy while maintaining reasonable computational cost. The Monte Carlo simulated annealing algorithm implemented in mcsqs was subsequently employed to optimize the atomic arrangement. During the optimization, atom swaps were performed iteratively to minimize the objective function measuring the difference between the supercell correlation functions and those of an ideal random alloy. Pair correlations up to the selected cutoff distance were explicitly matched, while higher-order clusters such as triplets and quadruplets were not included to minimize computational costs.
We performed multiple independent SQS calculations using different random initial configurations to avoid trapping in local minima, and the final SQS was selected based on the smallest residual correlation error relative to the ideal random alloy and the absence of significant systematic deviations in the low-order pair correlation functions. Particular emphasis was placed on accurately reproducing the first several nearest-neighbor shells, which contribute most significantly to the configurational energetics of substitutional alloys. Finally, the POSCAR file of the optimized structure was generated using the sqs2poscar utility, which served as the initial configuration for all first-principles calculations. Figure 1 shows the obtained supercell from the parent structure.

Structural optimizations and electronic structure calculations were carried out using density functional theory (DFT) within the projector augmented-wave (PAW) formalism, as implemented in the Vienna Ab initio Simulation Package (VASP). The exchange-correlation functional was treated using the generalized gradient approximation (GGA) of Perdew, Burke, and Ernzerhof (PBE). A 450 eV energy cutoff and Γ centered $2 \times 2 \times 2$ k-points was adopted for structure optimization,, and a $3 \times 3 \times 3$ for density of states calculations. Strong correlation effects of the rare-earth $4f$ electrons were treated using the DFT+U approach with U_{eff} values of 5.0 eV for Ce and 6.0 eV for both Nd and Pr. The atomic positions and lattice parameters were fully relaxed until the total energy and residual forces were smaller than 10^{-6} eV and -0.02 eV/Å, respectively. The valence electron configurations included in the PAW potentials were As ($4s^2 4p^3$), Ce_3 ($5s^2 5p^6 5d^1 6s^2$), Co_{pv} ($3p^6 3d^8 4s^1$), $Fe_p v$ ($3p^6 3d^7 4s^1$), La ($5s^2 5p^2 5d^1 6s^2$), Nd_3 ($5s^2 5p^6 5d^1 6s^2$), Pr_3 ($5s^2 5p^6 5d^1 6s^1$), Sb ($5s^2 5p^3$), Se ($4s^2 4p^4$), and Te ($5s^2 5p^4$).

The structural relaxation was performed allowing full optimization of both the cell volume and lattice degrees of freedom to obtain the ground-state geometry of the 136-atom SQS supercell. The resulting lattice vectors exhibited small deviations from the ideal cubic structure metric, which are attributed to the local chemical-environment

fluctuations inherent to a finite SQS representation of a chemically disordered alloy as well as the strain induced by the lattice mismatch in the As/Se/Sb/Te sublattice (*vide infra*). However, analysis of the converged stress tensor demonstrates that the relaxed configuration is mechanically equilibrated, with nearly isotropic diagonal stresses of 0.823, 0.919, and 0.847 kBar, negligible off-diagonal shear components (∼0.02 kBar), and a total external pressure of only 0.86 kBar. The maximum difference among the diagonal stress components is less than 0.1 kBar, indicating that no significant driving force remains for additional orthorhombic or shear distortions within the numerical accuracy of the DFT calculations. Therefore, the small symmetry-breaking distortions are interpreted as finite-cell configurational effects rather than evidence of a change in the underlying crystal symmetry.

In Figure 1, the relaxed geometry is presented alongside the starting geometry obtained from SQS ATAT. We observed that the geometry relaxation resulted in a contraction of the SQS supercell accompanied by a slight distortion from the ideal cubic symmetry. The fully optimized structure exhibits unequal lattice vectors with small off-diagonal lattice components, reflecting local strain induced by the random distribution of constituent elements. The supercell volume decreased from 6141.07 $Å^3$ to 5346.55 $Å^3$, corresponding to about 12.94% volume reduction. This corresponds to a reduction in the equivalent lattice parameter from 18.31 Åto 17.47 Å(4.6%). This volume contraction indicates that the starting lattice is energetically expanded relative to the DFT equilibrium configuration and that the chemically disordered alloy accommodates significant local atomic and strain relaxation induced by the chemical disorder introduced by the multicomponent SQS.

3 Results and Discussions

3.1 Formation Energy and Configurational Entropy

We begin by evaluating the formation energy of the reported HEIC phase. Using the relaxed energy of the supercell together with those of the constituent elements, ΔE_f can be determined based on the following equation:

$$\Delta E_f = E^{\text{atom}}_{\text{Supercell}} - \sum_i n_i E^{\text{atom}}_i, \tag{1}$$

where $E^{\text{atom}}_{\text{Supercell}}$ is the energy per atom, n_i is the atomic fraction of the i^{th} element, and E^{atom}_i is the energy per atom of the individual elemental reference. Using the obtained values of $E^{\text{atom}}_{\text{Supercell}} = -4.9679$ eV/atom and the values obtained from the relaxations of the constituent elements (See SI Table 1), we obtained a value of -0.17495 eV/atom, which corresponds to -2.9739 eV/f.u. We note that the observed negative formation energy, ΔE_f indicates the structure is energetically more stable than the separated constituent elements. Furthermore, if one approximates the enthalpy of mixing, ΔH_{mix} to be the DFT formation energy per atom referenced to elemental solids, we have a

value of −16.9 kJ/mol.
The configurational entropy, ΔS_{conf} is evaluated based on the equation:

$$\Delta S_{\text{conf}} = -R \sum_{i=1}^{n} x_i \ln x_i, \tag{2}$$

where R = 8.314 J/mol K is the universal gas constant, x_i is the atomic fraction of the i^{th} element, and n is the total number of constituent elements in the HEIC system. For proper understanding, we first evaluated the configurational entropy of the multicomponent Skutterudite by considering the chemical disorder independently on each crystallographic sublattice of $(La_{0.25}Ce_{0.25}Pr_{0.25}Nd_{0.25})(Fe_{0.5}Co_{0.5})_4(As_{0.25}Se_{0.25}Sb_{0.25}Te_{0.25})_{12}$. For the La/Ce/Pr/Nd, Fe/Co, and As/Se/Sb/Te sublattices, their contributions are 1.386R, 2.773R, and 16.64R per formula unit (f.u), respectively. Therefore, the observed total configurational entropy is (S_{conf}=20.79R) per formula unit, which then corresponds to (1.223R/f.u or (($\sim$ 10.17 $\text{J}, \text{mol}^{-1}, \text{K}^{-1}, \text{atom}^{-1}$)).Here we specifically note that the commonly cited value of 1.5R/atom criterion for high-entropy alloys (HEAs) of equiatomic elements or random substituted alloys does not generally hold here since HEICs generally feature multiple crystallographically distinct sublattices with different site multiplicities and degrees of chemical disorder. As such, normalizing the entropy per atom in such an instance makes it strongly dependent on the crystal structure and chemical distribution. Therefore, the observed value of 1.223R/atom configurational entropy in the reported material reflects substantial multisublattice chemical disorder and should be interpreted in the context of the Skutterudite structure rather than solely against the conventional 1.5R HEA criterion.

3.2 Lattice Mismatch and Valence Electron Concentration

The atomic-size mismatch parameter, δ, is a useful quantity that provides a quantitative measure of the size disparity among the constituent elements and can be used to quantify the degree of local lattice distortion expected in high-entropy materials. The atomic-size mismatch parameter, δ is given as:

$$\delta = 100 \sqrt{\sum_i c_i \left(1 - \frac{r_i}{\bar{r}}\right)^2}, \tag{3}$$

where the concentration-weighted average atomic radius, $\bar{r}$, is defined as

$$\bar{r} = \sum_i c_i r_i. \tag{4}$$

Here, c_i is the atomic fraction of element i, r_i is the atomic radius of element i, and $\bar{r}$ is the concentration-weighted average atomic radius. A larger δ would imply a greater deviation from an ideal lattice, which can enhance solid-solution strengthening and phonon scattering. For catalytic applications, in catalytic systems, a large δ can drive the modification of the local electronic structure and adsorption energetics. In the reported HEIC, we evaluated the values of δ as 1.06%, 2.33%, 7.37% for the RE(La/Ce/Pr/Nd), TM (Fe/Co), and PN (As/Se/Sb/Te) sublattices, respectively.

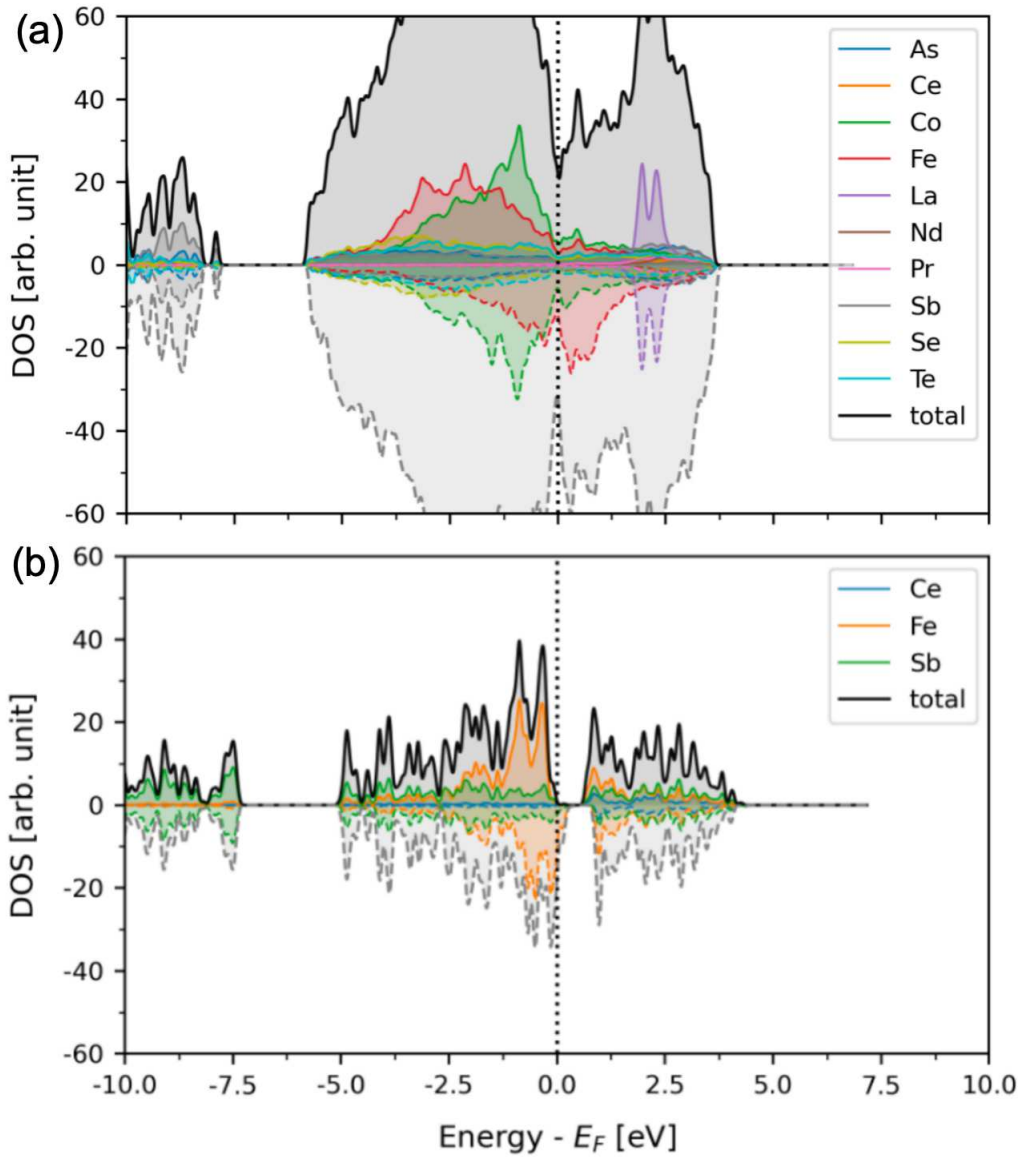


Fig. 2 TDOS of the (a) reported HEIC and (b) pristine $CeFe_4Sb_{12}$ in the energy range of -10.0 to 7.5 eV and showing the contributions from all the constituent elements. (b) TDOS of $CeFe_4Sb_{12}$ and also showing the contributions from Fe and Sb sublattices.

Here, the largest atomic-size mismatch is observed in the PN sublattice, which is driven by the significant difference in the atomic radius of Se and As as compared to those of Sb and Te.[48] Here, we expect such an observation to introduce a lattice distortion into the material, a feature which can be particularly important in certain

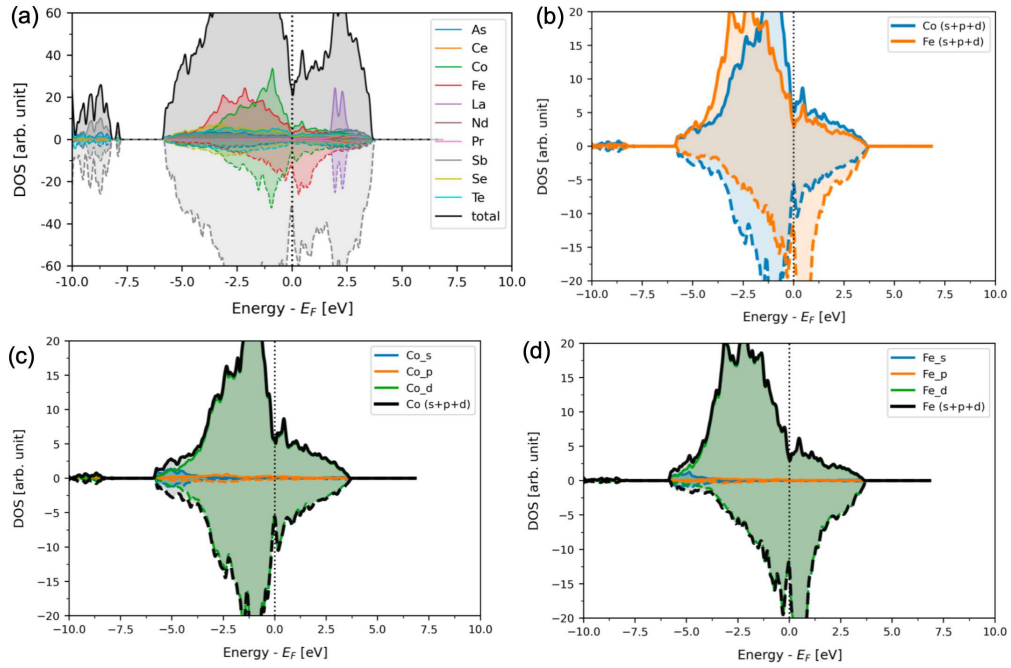


Fig. 3 (a) TDOS of the (a) reported HEIC. The partial DOS of (b) Co/Fe sublattice, (c) Co sublattice with orbital contributions, and (d) Fe sublattice with orbital contributions.

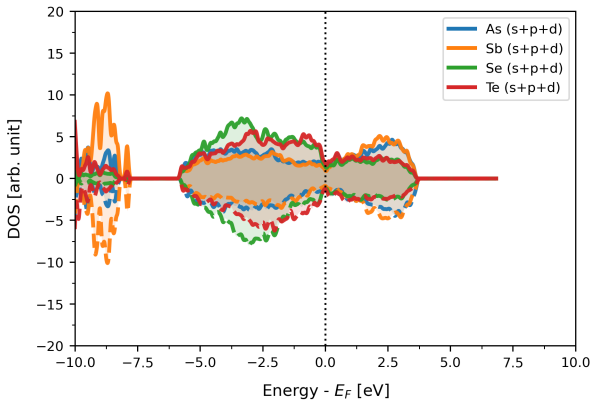


Fig. 4 Partial DOS of As/Se/Sb/Te sublattice of the reported HEIC. Color online.

high-entropy materials, since the randomly distributed atoms are expected to have different local environments with their associated bond lengths.[49, 50] In thermoelectrics, atomic-size mismatch as observed here can drive significant local strain fields and structural disorder that effectively scatter phonons.[51] We note that such observations would also have attendant effects in the mechanical properties of the

material, where it can help impede dislocation motion and improve thermodynamic stability.[52, 53]
The valence electron concentration (VEC), is another parameter that can be evaluated to gain additional insight into the electronic structure and phase stability of HEAs. It is given as VEC $= \sum_i c_i(\text{VEC})_i$, where c_i and $(\text{VEC})_i$ denote the atomic fraction and valence electron count of element i, respectively. The evaluated VEC for the reported HEIC is 6.06. We note that the VEC criterion for classifying HEAs into either BCC or FCC was mainly developed for the description of random solid-solution transition-metal HEAs and such a value would often classify the material to be in the BCC-favored regime. However, in our case, while the parent structure has a BCC–derived crystal structure, such a value places the material in a range of those having mixed bonding character.

3.3 Magnetism

The observed net moment per formula unit (f.u.) is about 3.88 μ_B/f.u for which the magnetic state is strongly Fe-dominated in what may be referred to as a transition-metal-driven ferrimagnet. Here, the largest local moments are on Fe atoms with values ranging from 0.35 to 2.93 μ_B and with 1.81 μ_B/atom indicating that Fe atoms sit in magnetically inequivalent local environments with varying magnetic moments. Such observation further supports the strong "local environment" effect in this case particularly in agreement with the observation in the pristine $CeFe_4Sb_{12}$ phase. [39, 40] The Co sublattice contributed only a small moment of 0.13 μ_B/atom, while the As/Se/Sb/Te sublattice shows mostly weak induced polarization. Contrary to what would normally be expected in a rare-earth-based system, the f-projected moments are essentially zero everywhere, with no sizable explicit $4f$ spin moment. This means the $4f$ electrons are not strongly spin-polarized in the converged state. Furthermore, the Fe-dominated magnetic state is further understood by comparing it with the moment of 2.20 μ_B/Fe, which is itinerant in nature. However, for localized high-spin Fe^{2+} or Fe^{3+} compounds, the values between 4.0-5.0 μ_B/Fe are typical; hence, it is plausible to consider that the magnetism in the reported HEIC phase is itinerant in nature.

3.4 Electronic Structure

In Figure 2, the density of states (DOS) of the HEIC phase and that of the pristine phase are presented in (a) and (b), respectively. In Figure 2 (a), the first feature to be observed is the huge DOS contributions near the Fermi level, which is conspicuous when compared to the contributions in the pristine phase in (b). This observation here possibly mean that many more electronic states become available for occupation. The DOS near the Fermi level is mostly dominated by Fe and Co in the valence band. For a clearer perspective, the DOS and the partial DOS of Fe and Co are shown in Figure 3. From (a) and (b), it appears that the contribution of Co dominates that of Fe in this region. In the conduction band, however, the contribution of the down-spin Fe dominates over that of Co. As may already be obvious, the various contributions

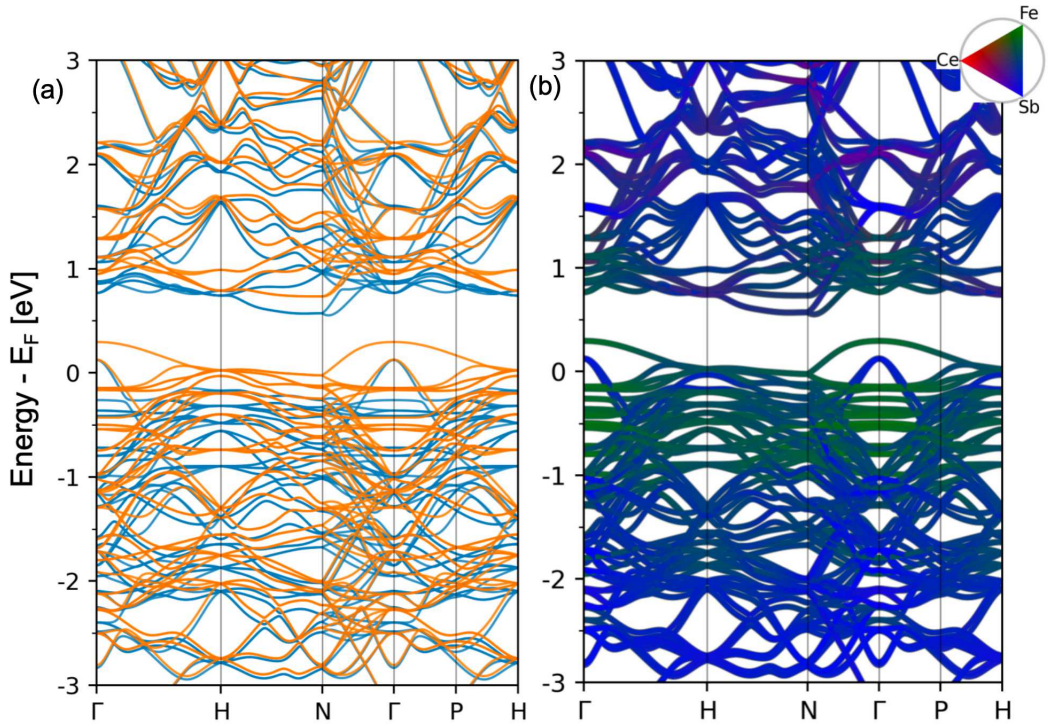


Fig. 5 (a) Spin polarized band structure of pristine $CeFe_4Sb_{12}$. (b) Band structure of pristine $CeFe_4Sb_{12}$ showing the contributions of each sublattice. (color online)

from Fe and Co are driven by their $3d$ orbitals as presented in (c) and (d) panels of Figure 3. Also, important to note that within the conduction band and in the energy window of ∼2.0 to 2.5 eV, La shows a significant contribution, in the region where the contributions from Fe and Co appear to decrease. Hence, contributions in the conduction band are dominated by Fe, Co, and La. This picture indicates that the $5d$ and $6s$ orbitals of La are more extended and hybridize with the $3d$ states of Fe and Co, forming delocalized conduction states. Such an observation is at variance with the other rare earth elements with partially filled $4f$ electrons and that are mostly localized. We further note that the observation in the pristine phase is consistent with earlier reports. [38]

Similarly, the contributions from the As/Se/Sb/Te sublattice are shown in Figure 4, and it is dominated by Se and Te near the Fermi level with comparable but lower contributions from As and Sb in the valence band. Similarly, contributions from Se and Te are also much higher within the conduction band in the 2.0 to 2.5 eV energy window. Intuitively, one can deduce that the observed large La DOS in the conduction band in this energy window (see Fig 2 (a) favors a stronger hybridization with the d orbitals of Fe/Co and the $p4$ orbitals of As/Se/Sb/Te,

thereby promoting orbital overlap and electronic localization. One other obvious observation from Figure 2 (*vide supra*) is also the evolution from semiconducting to metallic/semimetallic behavior. The pristine $CeFe_4Sb_{12}$ has a bandgap of ∼0.65 eV, and its DOS shows a hybridization between Fe 3*d* and Sb 5*p* states within the conduction band. However, the bandgap closed in the HEIC phase, leading to the overlap of the valence and conduction band. The key observations that manifest in here can be said to be driven by several factors. Here, strong hybridization and band broadening due to the presence of different atoms with different orbital energies as well as engineered chemical disorder that produces localized impurity states are likely responsible for the observed features. The various observation are therefore expected to drive an enhanced electrical conductivity and electronic specific heat. Also, the broad and asymmetric nature of DOS near the Fermi level is putatively expected to lead to the enhancement of electronic power factor in the material. We further expect that features like ferrimagnetism and the large DOS at the Fermi levels may also well provide for more electrons for pairing to drive a superconducting ground state, although that may not always be the case. Furthermore, tit is likely that the closing of the bandgap may also result in the reduction of the Seebeck coefficient and lost of carrier filtering, which may ultimately degrade the thermoelectric properties. Although oe may also expect that the increase in thermal conductivity if significant along with the expected low lattice thermal conductivity may ultimately compensate for the low Seebeck coefficient.

Figure 5 (a) shows the band structure of the pristine $CeFe_4Sb_{12}$ phase, which features the spin-up and spin-down data for the spin-polarized calculations. The spin-resolved electronic band structure provides insight into how the magnetic interactions influence the electronic states, and the difference between the two spin channels show the exchange splitting due to spin polarization, which indicates the presence of a local magnetic moment. Also important to note is the indirect bandgaps exhibited by the two channels which is consistent with previous reports. [38] Furthermore, in Figures 5 (b), the band structure reveals the contributions by each element, where regions near the valence band maximum are dominated by Fe contributions while the regions near the conduction band minimum feature contributions from the three constituent elements, with Sb been slightly dominant. For the HEIC phase, the raw band structure is presented in Figures 6 (a) and reveals diffused and broadened electronic band structure and the loss of sharp Bloch states. Such observation is however not unusual, since the introduction of multiple principal elements into the crystal lattice to develop the HEIC can generate substantial chemical disorder, thus producing local fluctuations in the crystal electrostatic potential. The observed feature is therefore the hallmark of HEIC, which is expected to contribute to the suppression of lattice thermal conductivity through enhanced phonon and electron scattering, increased electrical conductivity as well as reduced carrier mobility. Similarly, in Figures 6 (b), the unfolded band structure when compared with the pristine ones in Figures 5 exhibits well-pronounced spectral broadening with attendant loss of Bloch character as earlier noted for the raw band structure. The observation echoes the coupled effects of breakdown of translational symmetry and increased scattering of electronic

states caused by the random occupation of crystallographic sites by multiple elements in the developed HEIC and it is expected that such features will lead to significant suppression of the lattice thermal conductivity in this material.

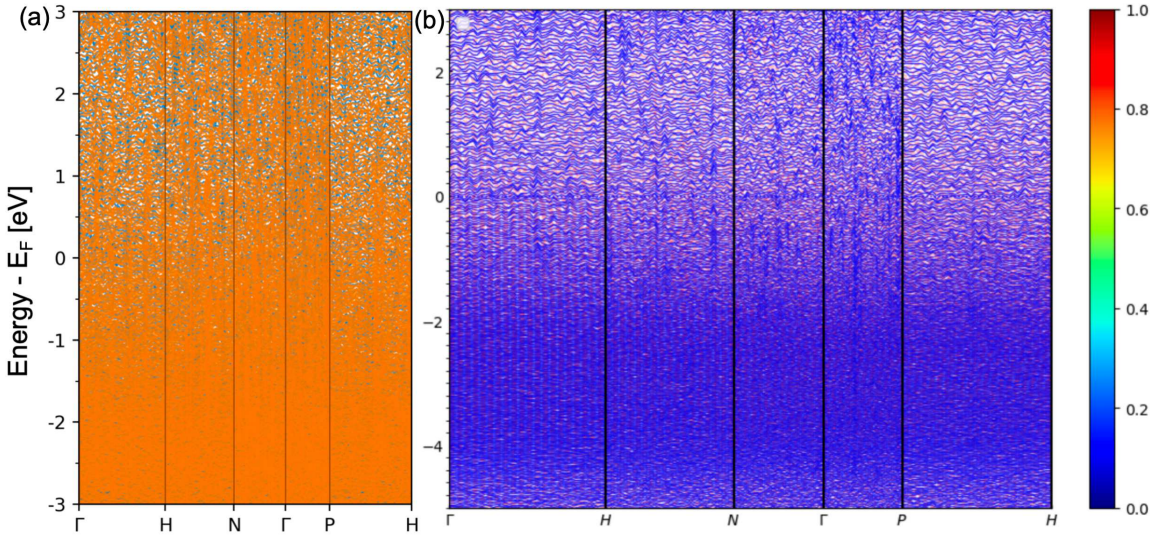


Fig. 6 (a) Raw band structure of the reported HEIC. (b) Unfolded band structure of the reported HEIC.

4 Discussion and Conclusion

We have reported on the design and computational studies of a high-entropy intermetallic compound to provide a viable materials landscape to explore several electronic and thermo-functional properties. The reported material $(La_{0.25}Ce_{0.25}Pr_{0.25}Nd_{0.25})(Fe_{0.5}Co_{0.5})_4(As_{0.25}Se_{0.25}Sb_{0.25}Te_{0.25})_{12}$, host several tuning knobs that can be leveraged to tailor the properties to various applications. Our studies essentially provides a groundbreaking work which we believe will generate significant interest in the direction of looking at the prospect of searching for high-entropy materials in caged structures.

We provide the configurational entropy of La/Ce/Pr/Nd, Fe/Co, and As/Se/Sb/Te sublattices, as well as that of the system. The evaluated entropy of 1.223R/f.u in the reported material is significant in the context of HEIC with strong site ordering. Additionally, the evaluation of the formation energy of -0.17495 eV/atom places the structure in the energetically favorable regime. The evaluated lattice mismatch is significant for the As/Se/Sb/Te sublattice with a value of 7.37%, which is driven by large atomic size difference between the various elements and consistent with the slight distortion from the ideal cubic symmetry observed in the relaxed structure.

However, we note that such an effect can induce local strain and structural disorder that may be beneficial for some thermoelectric applications and improved thermodynamic stability. The magnetism in this material is governed by the transition metal sublattice and is dominated by Fe, with Co contribution much smaller, as revealed by the observed moments and the DOS. The development of the HEIC is observed to close the bandgap and drive the material into a metallic-like material with overlapping bands at the Fermi level. The band structure features broadened electronic bands with the loss of sharp Bloch character, a feature that is reminiscent of a system with random occupation of crystallographic sites by multiple elements

Due to the significantly large number of atoms and prohibitively high computational cost, the current studies did not present the phonon studies, which would have been relevant to discussing the mechanical stability of the material. Perhaps subsequent work will leverage the use of machine learning tools to accomplish such an aspect. For the same reason, reliable transport properties calculations could not be carried out. Our preliminary attempt at calculating the transport properties produced some nonphysical results, which we attribute to the coarse k-points used for such calculations. We also anticipate that the experimental synthesis of this material will provide more opportunities to better study the various aspects of its thermodynamic and transport properties and will provide useful research directions in the development and synthesis of other HEICs.

Acknowledgment

MOO acknowledges financial support from XULA start-up fund. The NSF ACCESS program provided computational resources through the Anvil supercomputer at Purdue University under allocation PHY250050.

5 Author Contribution

MOO: Original conceptualization, research design, modeling and calculations, data collection, analysis, and prepared the figures. Wrote the original manuscript. All authors reviewed, edited and approved of the final version.

6 Conflict of Interest

The authors declare that they have no conflicts of interest.

References

[1] Y. Jien-Wei, Recent progress in high entropy alloys. ann. Chim. sci. Mat **31**(6), 633–648 (2006)

[2] D.B. Miracle, O.N. Senkov, A critical review of high entropy alloys and related concepts. Acta materialia **122**, 448–511 (2017)

[3] M.O. Ogunbunmi, S. Bobev, Exploiting the fraternal twin nature of thermoelectrics and topological insulators in zintl phases as a tool for engineering new efficient thermoelectric generators. Journal of Materials Chemistry C **11**(25), 8337–8357 (2023)

[4] E. Roduner, Understanding catalysis. Chem. Soc. Rev. **43**(24), 8226–8239 (2014)

[5] E.P. George, D. Raabe, R.O. Ritchie, High-entropy alloys. Nat. Rev. Mater. **4**(8), 515–534 (2019)

[6] S. Shafeie, S. Guo, Q. Hu, H. Fahlquist, P. Erhart, A. Palmqvist, High-entropy alloys as high-temperature thermoelectric materials. J. Appl. Phys. **118**(18) (2015)

[7] Y. Luo, S. Hao, S. Cai, T.J. Slade, Z.Z. Luo, V.P. Dravid, C. Wolverton, Q. Yan, M.G. Kanatzidis, High thermoelectric performance in the new cubic semiconductor agsnsbse3 by high-entropy engineering. J. Am. Chem. Soc. **142**(35), 15187–15198 (2020)

[8] Z. Ma, T. Xu, W. Li, Y. Cheng, J. Li, D. Zhang, Q. Jiang, Y. Luo, J. Yang, High entropy semiconductor agmngesbte4 with desirable thermoelectric performance. Adv. Funct. Mater. **31**(30), 2103197 (2021)

[9] Z. Ma, Y. Luo, J. Dong, Y. Liu, D. Zhang, W. Li, C. Li, Y. Wei, Q. Jiang, X. Li, et al., Synergistic performance of thermoelectric and mechanical in nanotwinned high-entropy semiconductors agmngepbsbte5. Advanced Materials **36**(45), 2407982 (2024)

[10] K. Li, L. Sun, W. Bai, N. Ma, C. Zhao, J. Zhao, C. Xiao, Y. Xie, High-entropy strategy to achieve electronic band convergence for high-performance thermoelectrics. J. Am. Chem. Soc. **146**(20), 14318–14327 (2024)

[11] Y. Wei, Z. Ma, W. Li, C. Li, B. Yang, C. Sun, S. Gang, W. Zhang, H. Long, X. Li, et al., A new n-type high entropy semiconductor agbipbse2s with high thermoelectric and mechanical properties. Adv. Funct. Mater. **34**(24), 2313719 (2024)

[12] R.Z. Zhang, F. Gucci, H. Zhu, K. Chen, M.J. Reece, Data-driven design of ecofriendly thermoelectric high-entropy sulfides. Inorg. Chem. **57**(20), 13027–13033 (2018)

[13] X. Wang, H. Yao, Z. Zhang, X. Li, C. Chen, L. Yin, K. Hu, Y. Yan, Z. Li, B. Yu, et al., Enhanced thermoelectric performance in high entropy alloys sn0. 25pb0. 25mn0. 25ge0. 25te. ACS Applied Materials & Interfaces **13**(16), 18638–18647 (2021)

[14] P. Koželj, S. Vrtnik, A. Jelen, S. Jazbec, Z. Jagličić, S. Maiti, M. Feuerbacher, W. Steurer, J. Dolinšek, Discovery of a superconducting high-entropy alloy. Phys. Rev. Lett. **113**(10), 107001 (2014)

[15] P. Sobota, R. Topolnicki, T. Ossowski, T. Pikula, A. Pikul, R. Idczak, Superconductivity in the high-entropy alloy (nbta) 0.67 (mohfw) 0.33. Phys. Rev. B **106**(18), 184512 (2022)

[16] S. Marik, K. Motla, M. Varghese, K. Sajilesh, D. Singh, Y. Breard, P. Boullay, R. Singh, Superconductivity in a new hexagonal high-entropy alloy. Phys. Rev. Mater. **3**(6), 060602 (2019)

[17] Y. Mizuguchi, Superconductivity in high-entropy-alloy telluride aginsnpbbite5. J. Phys. Soc. Jpn. **88**(12), 124708 (2019)

[18] N. Ishizu, J. Kitagawa, New high-entropy alloy superconductor hf21nb25ti15v15zr24. Results Phys. **13**, 102275 (2019)

[19] W.L. Nelson, A. Chemey, M. Hertz, E. Choi, D.E. Graf, S. Latturner, T. Albrecht-Schmitt, K. Wei, R.E. Baumbach, Superconductivity in a uranium containing high entropy alloy. Sci. Rep. **10**(1), 4717 (2020)

[20] J. Kitagawa, K. Hoshi, Y. Kawasaki, R. Koga, Y. Mizuguchi, T. Nishizaki, Superconductivity and hardness of the equiatomic high-entropy alloy hfmonbtizr. J. Alloys Compd. **924**, 166473 (2022)

[21] A. Yamashita, T.D. Matsuda, Y. Mizuguchi, Synthesis of new high-entropy alloy-type nb3 (al, sn, ge, ga, si) superconductors. J. Alloys Compd. **868**, 159233 (2021)

[22] X. Zhang, N. Winter, C. Witteveen, T. Moehl, Y. Xiao, F. Krogh, A. Schilling, F.O. von Rohr, Preparation and characterization of high-entropy alloy (tanb) 1-x (zrhfti) x superconducting films. Phys. Rev. Res. **2**(1), 013375 (2020)

[23] Y. Mizuguchi, M.R. Kasem, T.D. Matsuda, Superconductivity in cual2-type co0. 2ni0. 1cu0. 1rh0. 3ir0. 3zr2 with a high-entropy-alloy transition metal site. Mater. Res. Lett. **9**(3), 141–147 (2021)

[24] K. Stolze, J. Tao, F.O. Von Rohr, T. Kong, R.J. Cava, Sc–zr–nb–rh–pd and sc–zr–nb–ta–rh–pd high-entropy alloy superconductors on a cscl-type lattice. Chem. of Mater. **30**(3), 906–914 (2018)

[25] S. Nellaiappan, N.K. Katiyar, R. Kumar, A. Parui, K.D. Malviya, K. Pradeep, A.K. Singh, S. Sharma, C.S. Tiwary, K. Biswas, High-entropy alloys as catalysts for the co2 and co reduction reactions: experimental realization. ACS Catal. **10**(6), 3658–3663 (2020)

[26] H. Li, Y. Han, H. Zhao, W. Qi, D. Zhang, Y. Yu, W. Cai, S. Li, J. Lai, B. Huang, et al., Fast site-to-site electron transfer of high-entropy alloy nanocatalyst driving redox electrocatalysis. Nat. Commun. **11**(1), 5437 (2020)

[27] M. Sahlberg, D. Karlsson, C. Zlotea, U. Jansson, Superior hydrogen storage in high entropy alloys. Sci. Rep. **6**(1), 36770 (2016)

[28] P. Edalati, R. Floriano, A. Mohammadi, Y. Li, G. Zepon, H.W. Li, K. Edalati, Reversible room temperature hydrogen storage in high-entropy alloy tizrcrmnfeni. Scr. Mater. **178**, 387–390 (2020)

[29] K.R. Cardoso, V. Roche, A.M. Jorge Jr, F.J. Antiqueira, G. Zepon, Y. Champion, Hydrogen storage in mgaltifeni high entropy alloy. J. Alloys Compd. **858**, 158357 (2021)

[30] R. Floriano, G. Zepon, K. Edalati, G.L. Fontana, A. Mohammadi, Z. Ma, H.W. Li, R.J. Contieri, Hydrogen storage properties of new a3b2-type tizrnbcrfe high-entropy alloy. Int. J. Hydrogen Energy **46**(46), 23757–23766 (2021)

[31] X. Wang, W. Guo, Y. Fu, High-entropy alloys: emerging materials for advanced functional applications. J. Mater. Chem. A **9**(2), 663–701 (2021)

[32] L.Y. Li, M. Zhang, M. Jiang, L.H. Gao, Z. Ma, M.S. Cao, High entropy ceramics for electromagnetic functional materials. Adv. Funct. Mater. **35**(10), 2416673 (2025)

[33] M. Rull-Bravo, A. Moure, J. Fernández, M. Martín-González, Skutterudites as thermoelectric materials: revisited. Rsc Adv. **5**(52), 41653–41667 (2015)

[34] G.S. Nolas, *The physics and chemistry of inorganic clathrates* (Springer, 2014)

[35] T. Onimaru, K. T. Matsumoto, Y. F. Inoue, K. Umeo, Y. Saiga, Y. Matsushita, R. Tamura, K. Nishimoto, I. Ishii, T. Suzuki, et al., Superconductivity and structural phase transitions in caged compounds rt2zn20 (r= la, pr, t= ru, ir). J. Phys. Soc. Jpn. **79**(3), 033704 (2010)

[36] M.O. Ogunbunmi, B.M. Sondezi, H.S. Nair, A.M. Strydom, Electronic and magnetic properties of quasi-skutterudite prco2ga8 compound. Phys. B: Condens. Matter **536**, 128–132 (2018)

[37] M.O. Ogunbunmi, A.M. Strydom, Promising thermoelectric properties of heavy-fermion semimetal pr3os4ge13. J. Phys.: Condens. Matter **32**(40), 405606 (2020)

[38] K. Nouneh, A.H. Reshak, S. Auluck, I.V. Kityk, R. Viennois, S. Benet, S. Charar, Band energy and thermoelectricity of filled skutterudites lafe4sb12 and cefe4sb12. J. Alloys Compd. **437**(1–2), 39–46 (2007). https://doi.org/10.1016/j.jallcom.2006.07.114

[39] R. Viennois, D. Ravot, J.C. Tedenac, S. Charar, A. Mauger, Magnetic properties of $ce_yfe_{4-x}ni_xsb_{12}$. Mater. Sci. Eng B **119**(1), 1–12 (2005)

[40] D. Bérardan, E. Alleno, C. Godart, Rare earth valence and paramagnetic properties of the skutterudites $ce_{1-z}yb_zfe_4sb_{12}$, $ba_yfe_4sb_{12}$ and $la_yfe_4sb_{12}$. J. of Magn. and Magn. Mater. **285**(1–2), 245–253 (2005). https://doi.org/10.1016/j.jmmm.2004.07.047

[41] R. Viennois, L. Girard, D. Ravot, S. Paschen, S. Charar, A. Mauger, P. Haen, J. Tedenac, Thermoelectric properties of ce (la) fe 4 sb 12 skutterudites under a magnetic field. Phys. Rev. B **80**(15), 155109 (2009)

[42] I. Ishii, T. Suzuki, T. Fujita, I. Mori, H. Sugawara, M. Yoshizawa, Y. Nemoto, T. Goto, *Ultrasonic dispersion in the filled skutterudite CeFe4Sb12*, in . *Phys. Conf. Ser.*, vol. 150 (2009), p. 042071

[43] K.i. Magishi, H. Sugawara, M. Takahashi, T. Saito, K. Koyama, T. Saito, S. Tatsuoka, K. Tanaka, H. Sato, Effects of filling fraction on magnetic properties of filled skutterudite r fe4sb12 (r= la, ce) synthesized under high pressure. J. Phys. Soc. Jpn. **81**(12), 124706 (2012)

[44] G.J. Long, D. Hautot, F. Grandjean, D.T. Morelli, G.P. Meisner, Mössbauer effect study of filled antimonide skutterudites. Phys. Rev. B **60**(10), 7410 (1999)

[45] X. Xia, P. Qiu, X. Huang, S. Wan, Y. Qiu, X. Li, L. Chen, Oxidation behavior of filled skutterudite cefe4sb12 in air. J. Electron. Mater. **43**(6), 1639–1644 (2014)

[46] E. Bauer, R. Chau, N. Dilley, M. Maple, D. Mandrus, B. Sales, Pressure dependence of the electrical resistivity of the filled skutterudites lnfe4sb12 (ln= ce, yb). J. Phys. Condens. Matter **12**(7), 1261–1267 (2000)

[47] M. Lebeda, J. Drahokoupil, P. Vlčák, Š. Svoboda, A. van de Walle, Simplysqs: An automated and reproducible workflow for special quasirandom structure generation with atat. J. of Comp. Sci. **96**, 102846 (2026). https://doi.org/10.1016/j.jocs.2026.102846

[48] R.D. Shannon, Revised effective ionic radii and systematic studies of interatomic distances in halides and chalcogenides. Acta Crystallogr. A **32**(5), 751–767 (1976). https://doi.org/10.1107/S0567739476001551

[49] H. Wang, Q. He, X. Gao, Y. Shang, W. Zhu, W. Zhao, Z. Chen, H. Gong, Y. Yang, Multifunctional high entropy alloys enabled by severe lattice distortion. Adv.Mater. **36**(17), 2305453 (2024)

[50] Z. An, S. Mao, Y. Liu, L. Wang, H. Zhou, B. Gan, Z. Zhang, X. Han, A novel hfnbtativ high-entropy alloy of superior mechanical properties designed on the principle of maximum lattice distortion. J. Mater. Sci. Technol. **79**, 109–117

(2021)

[51] S. Liu, D. Wu, M. Kong, W. Wang, L. Xie, J. He, High-entropy thermoelectric materials: advances, challenges, and future opportunities. ACS Energy Lett. **10**(2), 925–934 (2025)

[52] H. Song, F. Tian, Q.M. Hu, L. Vitos, Y. Wang, J. Shen, N. Chen, Local lattice distortion in high-entropy alloys. Phys. Rev. Mater. **1**(2), 023404 (2017)

[53] C. Lee, Y. Chou, G. Kim, M.C. Gao, K. An, J. Brechtl, C. Zhang, et al., Lattice-distortion-enhanced yield strength in a refractory high-entropy alloy. Adv. Mater. **32**(49), 2004029 (2020)